Enhanced strength-ductility synergy of a partially recrystallized $Al_6Cr_{25}Fe_{34}Ni_{35}$ multi-principal element alloy

Kaiju Lu [a,*], Hao Shi [b,c,**], Alfons Weisenburger [b], Jarir Aktaa [a]

[a] Institute for Applied Materials (IAM), Karlsruhe Institute of Technology (KIT), Hermann-von-Helmholtz-Platz 1, 76344 Eggenstein Leopoldshafen, Germany
[b] Institute for Pulsed Power and Microwave Technology (IHM), Karlsruhe Institute of Technology (KIT), Hermann-von-Helmholtz-Platz 1, 76344 Eggenstein-Leopoldshafen, Germany
[c] Max-Planck-Institut für Eisenforschung (MPIE), 40237 Düsseldorf, Germany

ARTICLE INFO

Keywords:
Multi-principal element alloy (MPEA)
Mechanical properties
Deformation mechanism
Dislocation

ABSTRACT

Co-free and Al-alloyed FCC multi-principal element alloys (MPEAs) have attracted increasing interest due to their low-cost, high potential to show excellent corrosion/oxidation resistance and mechanical properties. Here we report the mechanical deformation behavior of a single face-centered cubic (FCC) and partially recrystallized $Al_6Cr_{25}Fe_{34}Ni_{35}$ (at.%, AlCrFeNi) MPEA at room temperature and 550 °C with comparisons to other model MPEAs (including CoCrFeMnNi, CoCrNi and CrFeNi). The AlCrFeNi alloy exhibits higher strength-ductility synergy than the CoCrFeMnNi MPEA tested at the same conditions, especially at elevated temperature. Besides, it also shows higher yield strength than the CoCrNi and CrFeNi MPEAs. Microstructural investigations unveiled that, the deformed microstructures manifest a high density of dislocations (in the form of tangles and walls/cells). These tangles and walls/cells contributed to the AlCrFeNi's stage I and II strain hardening behaviors, respectively, as well as to the enhanced strength-ductility synergy. Further analyses also pinpointed the origins of higher yield strength in AlCrFeNi than in other MPEAs.

1. Introduction

In the last two decades, multi-principal element alloys (MPEAs), consisting of 3 to 5 principal elements (each with atomic ratio of 5% - 35%), have triggered numerous pursuits due to their unique atomic structures [1–7]. Some of the face-centered cubic (FCC) MPEAs (such as CoCrFeMnNi, CrFeNi, and CoCrNi) have shown excellent combination of mechanical properties, namely high strain hardening rate, ductility [8–12], fatigue crack growth resistance [13], low-cycle fatigue resistance [14–16] and fracture toughness [17,18]. However, despite having outstanding strength and ductility at cryogenic temperatures, FCC MPEAs exhibit limited strength at room temperature (RT) and elevated temperatures [9–11]. Hence, immense efforts have been devoted to improve their strength, such as by adding additional solid solution elements (*e.g.*, Al, Ti and Ta) [7,19–21] and introducing heterogenous (or partially recrystallized) microstructures [22–24]. Besides, most of these MPEAs are designed by alloying with a large amount of expensive Co element, and the immense increase in cost largely limits their commercialization. In addition, Co is an undesired element for many applications, e. g. in nuclear application due to its high activation.

Recently, the Co-free and less-expensive FCC Cr-Fe-Ni alloys, due to their similarity to modern austenitic stainless steels and Fe-based superalloys, have been considered as a cornerstone of these engineering alloys [11]. For instance, the equiatomic CrFeNi MPEA was demonstrated to show excellent strength-ductility combination and the largest grain boundary strengthening capability as compared to other equiatomic alloys from the Co-Cr-Fe-Mn-Ni system [11]. Furthermore, by introducing a certain amount of Al, the non-equiatomic Al-alloyed Cr-Fe-Ni system alloys (*e.g.*, $Al_6Cr_{25}Fe_{34}Ni_{35}$, at.%), which maintains a single face-centered cubic (FCC) solid solution structure, have been reported to possess excellent corrosion/oxidation resistance to varying aggressive environments (*e.g.*, molten Pb, high temperature steam) [25]. This is mainly attributed to the *in-situ* formation of an Al_2O_3-based protective oxide layer on alloy surface at the exposed conditions [25]. These intriguing features render the non-equiatomic Al-Cr-Fe-Ni alloys promising candidates in high temperature applications, whereas there is

* Corresponding author.
** Corresponding author at: Institute for Pulsed Power and Microwave Technology (IHM), Karlsruhe Institute of Technology (KIT), Hermann-von-Helmholtz-Platz 1, 76344 Eggenstein-Leopoldshafen, Germany.
E-mail addresses: kaiju.lu@hotmail.com, kaiju.lu@kit.edu (K. Lu), h.shi@mpie.de (H. Shi).

a lack of understanding of their mechanical properties.

Consequently, the current work aims to reveal mechanical behaviors and deformation mechanisms of a partially recrystallized $Al_6Cr_{25}Fe_{34}Ni_{35}$ MPEA at RT and a typical elevated temperature (550 °C). Moreover, the obtained results will be compared to other FCC model MPEAs (such as CoCrFeMnNi, CoCrNi and CrFeNi) to identify potential unique features of the AlCrFeNi alloy.

2. Material and methods

2.1. Material

The investigated $Al_6Cr_{25}Fe_{34}Ni_{35}$ (in atomic ratio, denoted as AlCrFeNi hereafter) MPEA was synthesized from high purity elemental bulk materials (with at least 99.95% purity), which were arc melted at least five times and cast under Ar atmosphere into a water chilled Cu mold. The cooling rate of the current arc melting system (MAM-1, Serial-No.2426220) is around 100 K/s between 2300 K and 1300 K. The as-cast ingot was subjected to cold rolling with 80% thickness reduction down to 2 mm in thickness.

2.2. Tensile testing

Flat dog-bone shaped micro-specimens (with gauge length, width, and thickness: 1.5 mm, 0.3 mm, and 0.12 mm, respectively [10]) were fabricated from the above-mentioned cold-worked material by micro-electric discharge machining, with their tensile axes parallel to the rolling direction. Before testing, all specimens were annealed at an Austenitization temperature (950 °C for 5 min) according to equilibrium phase calculation (performed by Thermo-Calc, TCHEA4 database), followed by water-quenching to ensure a partially-recrystallized microstructure.

Uniaxial micro-tensile tests were performed in air using an in-house micro-tensile testing setup, for which more details can be found in Refs. [10]. The tensile tests were carried out in air under a constant strain rate of 3×10^{-4} s^{-1} at RT and 550 °C. The 550 °C was chosen as it represents a typical service temperature in elevated temperature applications, *e.g.*, power plants [15]. The tests at each condition were repeated at least twice to ensure reproducibility. Notably, it has been proven that the micro-tensile tests can provide comparable mechanical properties, in terms of yield strength (YS), ultimate tensile strength (UTS) and uniform elongation (UE) [10], as compared to their macro-scale counterparts [26].

2.3. Microstructure characterization

To reveal underlying deformation mechanisms, electron back-scattered diffraction (EBSD), electron channeling contrast imaging (ECCI) and transmission electron microscope (TEM) investigations were performed. For EBSD, both as-annealed and post-deformed samples were mechanically ground and then polished using 9, 3, and 1 μm water-based diamond suspensions and finally using 50 nm colloidal silica suspension on a vibratory polisher. The EBSD orientation imaging was scanned using an FEI Nova dual-beam scanning electron microscope (SEM) equipped with an HKL Channel 5 EBSD detector (operating at 20 kV and a step size of 0.25 μm. Then the EBSD raw data were processed and analyzed, *via* EDAX's OIM software, to obtain Inverse Pole Figure (IPF) and Kernel Average Misorientation (KAM) maps. The KAM values can qualitatively reflect geometrically necessary dislocation (GND) density. Here, KAM values were obtained by averaging the misorientation among one point and its first-neighboring points. Neighboring points with misorientation exceeding 5° were excluded from the kernel.

Furthermore, the EBSD samples were scanned by the ECCI technique using a ZEISS Merlin SEM (at 30 kV and 2 nA current) to visualize the dislocations involved before and after deformation. The ECCI, working in a two-beam condition (*i.e.*, a transmitted beam and a beam diffracted with the Bragg angle), has an advantage of characterizing a relatively large surface area. Besides, conventional bright-field (BF) TEM imaging was also carried out using an FEI TECNAI-20F microscope at 200 kV. The TEM sample was prepared by focused ion beam milling using the above-mentioned SEM at 30 kV and polished at 5 kV and different currents. Additionally, the fracture surface of the tested samples was also examined *via* the abovementioned SEM.

3. Results and discussion

3.1. Microstructures before deformation

Typical microstructures of the as-annealed AlCrFeNi alloy are provided in Fig. 1. The IPF map along the rolling direction (overlaying with image quality (IQ) map, Fig. 1a), and KAM map (Fig. 1b) reveal that the as-annealed microstructure exhibits partially recrystallized grains (with average grain sizes of ~7 ± 3 μm). Specifically, the recrystallized grains have a low dislocation density (*see* Fig. 1c, also *see* blue regions in Fig. 1b with low KAM values). Moreover, the fraction of recrystallized grains is estimated to be ~75 ± 3% (standard error). Whereas, the rest non-recrystallized grains contain a relatively high density of dislocations, *see* Fig. 1d and green regions in Fig. 1b with high KAM values. Besides, the randomly-distributed colors of grains (Fig. 1a) suggest no evident texture. The observed high density of annealing twins (Fig. 1a) imply the alloy's low-to-medium stacking fault energy [10].

3.2. Stress-strain behavior

Fig. 2a and b show the uniaxial engineering stress-strain curves of the AlCrFeNi MPEA tested at RT and 550 °C, respectively. The obtained values of the YS, UTS and UE are listed in Table 1. Evidently, at RT, the AlCrFeNi yields at ~456 MPa (YS), reaching a UTS of ~685 MPa and a UE of ~22% (Fig. 2a) until local necking occurs. At 550 °C, the YS, UTS and UE decrease to ~324 MPa, ~517 MPa and ~20%, respectively (Fig. 2b). Furthermore, the excellent ductility (UE) of the alloy tested at both temperatures can be supported by the observed numerous dimples on the fracture surfaces, as an indication of ductile fracture (*e.g.*, *see* the insets of Fig. 2a). In addition, at 550 °C, serrated plastic deformation occurs (Fig. 2b), which is similar to CoCrFeMnNi and is related to dynamic strain aging behavior [10].

For comparison, the corresponding curves/values of a comparable grain-sized (~ 7 μm) FCC CoCrFeMnNi MPEA tested at the same conditions [10] are also given in Fig. 2 and Table 1. It can be seen that, as compared to CoCrFeMnNi alloy, the AlCrFeNi alloy exhibits higher YS and UTS, as well as comparable (or if any, only modest compromise to) ductility at RT and 550 °C (Table 1). Especially, the YS of the AlCrFeNi increases by ~35% and ~ 47% at RT and 550 °C as compared to that of CoCrFeMnNi.

In addition, the YS of AlCrFeNi alloy is also ~27% higher than that of the equiatomic CoCrNi and CrFeNi MPEAs (*e.g.*, both ~360 MPa [8,11]) at RT (Table 1).

The strain-hardening rate (SHR, *i.e.*, derivative of true stress) *versus* true stress curves of AlCrFeNi at RT and 550 °C are plotted in Fig. 3a. At both temperatures, a decreasing trend of SHR is observed until necking occurs (*i.e.*, Considere's criterion is fulfilled) (Fig. 3a). Moreover, based on the decreasing rate of SHR, the curves can be further divided into two stages, namely stage I (with rapid decrease) and stage II (with relatively slow decrease). The transition region (between stage I and stage II) lies at the true strain of ~5% - 7%, depending on the temperature.

The SHR *versus* true stress curves of CoCrFeMnNi were also shown in Fig. 3b for comparison. At 550 °C, the AlCrFeNi exhibits higher SHR values than CoCrFeMnNi; whereas, at RT, the AlCrFeNi shows higher values at stage I but lower values at stage II (*i.e.*, when true stress is >600 MPa), *see* Fig. 3b. This observation suggests the AlCrFeNi's high initial strain hardening ability, which is ascribed to the initial high

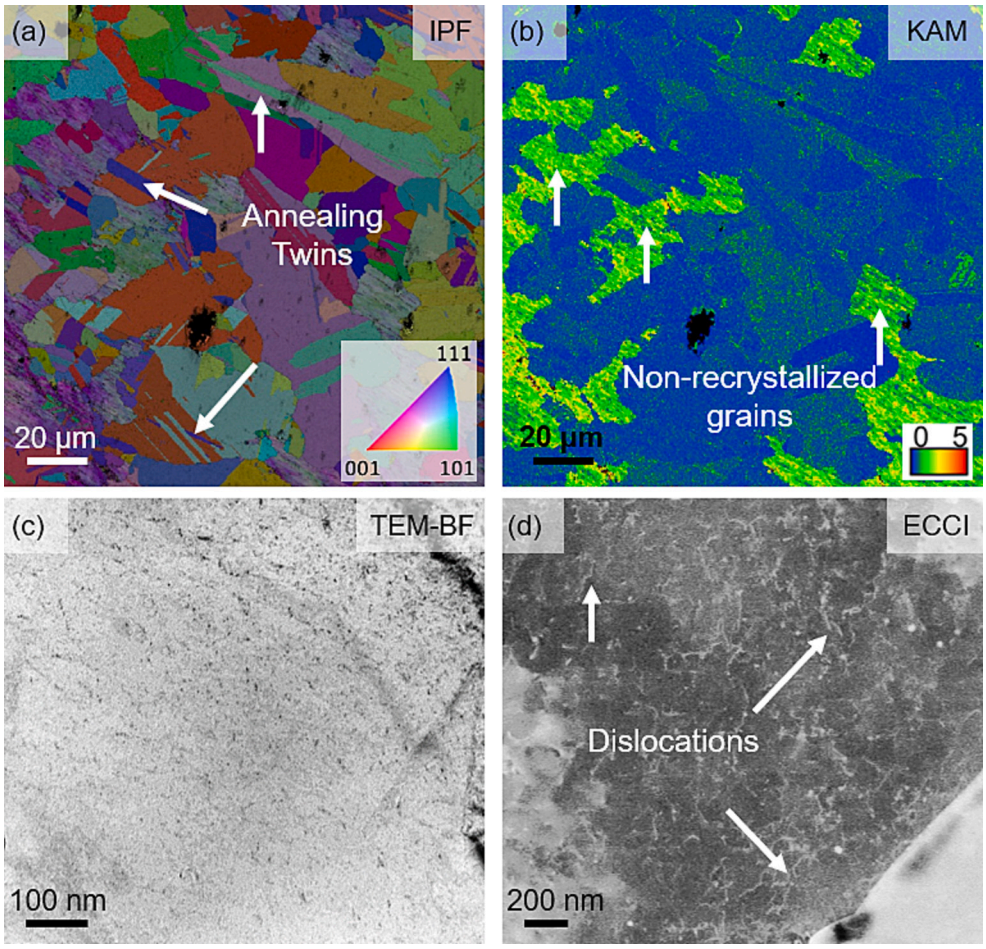

Fig. 1. Microstructures of the AlCrFeNi alloy at the as-annealed state: (a) IPF overlaying with IQ map, (b) KAM map, (c) TEM-BF micrograph from a recrystallized grain and (d) ECCI micrograph from a non-recrystallized grain.

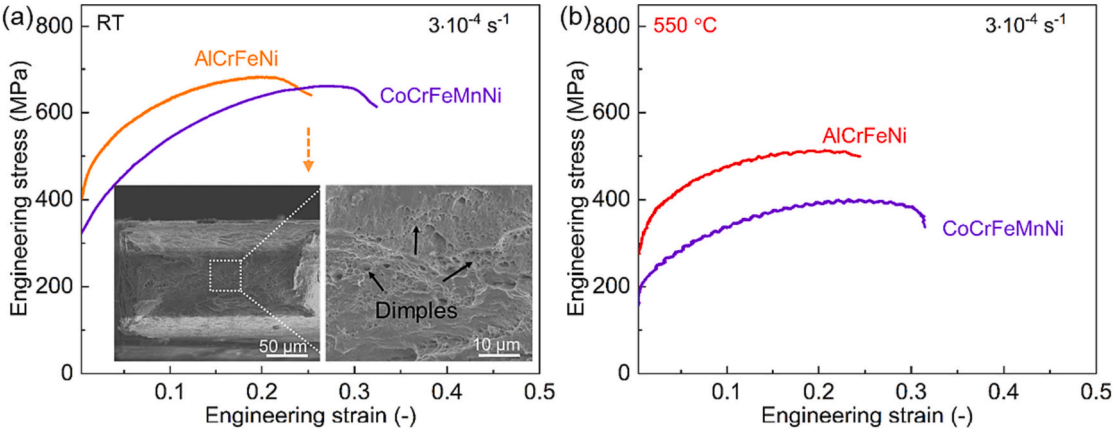

Fig. 2. Representative tensile engineering stress-strain curves of the AlCrFeNi alloy tested at (a) RT and (b) 550 °C. The insets of (a) are typical SEM micrographs from the fracture surface of AlCrFeNi alloy tested at RT. Notably, the fracture surface at 550 °C is similar to that at RT. For comparison, the results of CoCrFeMnNi [10] were also shown here for comparison.

dislocation density in the non-recrystallized regions (Fig. 1b).

3.3. Deformation mechanisms

To unravel the reasons for the stress-strain behaviors, operating deformation mechanisms were characterized *via* EBSD and ECCI. IPF maps and corresponding KAM maps of AlCrFeNi samples tested at RT and 550 °C till fracture were shown in Fig. 4. As compared to the as-annealed state (Fig. 1a), the IPF maps indicate no noticeable change in grain sizes, texture and twin boundaries (Fig. 4a and c). Besides, no additional phases or precipitates formed after deformation at RT and 550 °C. Nevertheless, by comparing the KAM maps, more green-colored grains can be observed after deformation (Fig. 4b and d) than before (Fig. 1b). This observation indicates higher KAM values and GND

Table 1
Uniaxial tensile properties of the AlCrFeNi alloy and comparisons to CoCrFeMnNi [10], CoCrNi [8] and CrFeNi [11].

Materials	Temperature	Yield strength, YS (MPa)	Ultimate tensile strength, UTS (MPa)	Uniform elongation, UE
AlCrFeNi	RT	456 ± 9	685 ± 3	(22 ± 2)%
	550 °C	324 ± 6	517 ± 4	(20 ± 3)%
CoCrFeMnNi	RT	~ 338	~ 670	~ 25%
	550 °C	~ 220	~ 400	~ 24%
CoCrNi	RT	~ 360	~ 870	~38%
CrFeNi	RT	~ 360	-	-

Here, the - symbol indicates that corresponding data are not available.

densities after tension loading (than before). Furthermore, the KAM values at 550 °C are lower than those at RT. This is related to more dislocations cross slip induced annihilation (*i.e.*, dynamic recovery) at 550 °C [10]. Moreover, both recrystallized and non-recrystallized grains manifest larger KAM values than before (*compare* arrow indicated regions in, Fig. 4b and d to that in Fig. 1b), suggesting that all grains participated in the deformation.

To provide high-resolution information on the deformed microstructures, typical ECCI micrographs of AlCrFeNi alloy tested at RT were shown in Fig. 5. The typical deformed features are manifested by high density of dislocation tangles (Fig. 5a) and dislocation walls/cells (Fig. 5b-c). This observation is believed to be also valid for those tested at 550 °C, according to similar results obtained from CoCrFeMnNi [27,28]. Furthermore, as this AlCrFeNi alloy is depleted of Co element that usually promotes HCP phase formation and decreases the SFEs of alloys, the dislocations in this deformed alloy are expected to be more of full character. Additionally, no deformation twins (DTs) were detected *via* ECCI, indicating DTs' insignificant role (if any) in the mechanical properties of the present AlCrFeNi alloy. Indeed, in this AlCrFeNi alloy, there is no strain hardening plateau, which is usually believed to mark the onset of DTs [8]. This is in line with the findings for CoCrFeMnNi that only a minor fraction of DTs was present at RT [10]; instead, dislocation cells dominated at large strains (*e.g.*, 20%) at RT and above [9,28].

In light of the deformation microstructures, the reasons for the strain hardening stages I and II (Fig. 3) can be illustrated as follows. In the fine-grained AlCrFeNi, deformation initially occurred in the recrystallized 'soft' grains. It is well-accepted that dislocations from multiple (at least five independent) slip systems are activated to fulfill the von-Mises Criterion and ensure compatible deformation with the neighboring grains [29]. Dislocations from different slip systems meet each other and form dislocation tangles or locks (Fig. 5a) which contribute to strain hardening. As the applied stress increases at the initial stage, the number of grains (that participated in the deformation) gradually increases, as the critical stress in these grains is exceeded [30]. Hence, the number of 'soft' grains decreases and the strain hardening rate/capability decreases (*i.e.*, stage I in Fig. 3a).

With further increasing strains, most grains exhibit high density of dislocations. As stress further increases, dislocations start to organize into low-energy substructures, such as Taylor lattice and walls/cells (Fig. 5b-c). These substructures are generally believed to induce pronounced long-range back-stress, rendering dislocations (within the channels between walls) difficult to transmit across them and leading to an altered slope in the work-hardening response (stage II in Fig. 3a) [4,31–34]. On the other hand, the dislocation substructures, especially walls/cells formed due to dynamic recovery process, provide free path for mobile dislocations [14,34]. Therefore, the strain hardening rate still decreases in stage II.

Interestingly, the dislocation cells formation and dynamic recovery have been previously related to stage I strain hardening [35,36]. However, in CoCrFeMnNi, dislocation slip bands and wall/cell substructures were reported to be prevalent at small (2.1%) and large (20%) strains, respectively, which are corresponding to stage I and II deformations [9,28]. This finding is anticipated to be applicable to the present AlCrFeNi alloy. Therefore, it is suggested that the wall/cell substructures contributed more to stage II (than stage I) strain hardening behavior in this study.

Additionally, it was reported that stage II strain hardening is related to DTs formation in CoCrNi [22]. Despite the absence of apparent DTs, the high strain hardening rate (from dislocation substructures alone) postpones strain localization, which ensures high strength-ductility combination of this AlCrFeNi alloy.

Furthermore, to compare the contributions of solid solution strengthening and grain boundary strengthening to the high YS of the AlCrFeNi alloy (Table 1), the available Hall-Petch parameters σ_0 and k_y of CrFeNi [11], CoCrNi [37] and CoCrFeMnNi [28] are listed in Table 2.

It can be seen that, as compared to CoCrFeMnNi and CoCrNi alloys, the equiatomic CrFeNi exhibits lower intrinsic σ_0 (or solid solution strengthening) but higher k_y [11]. Due to the similar compositions between CrFeNi and current AlCrFeNi, it is relatively reasonable to assume that the AlCrFeNi may also manifest lower σ_0 and higher k_y than CoCrFeMnNi and CoCrNi. Therefore, despite the lower σ_0, the above-mentioned higher strain hardening ability (Fig. 3b) and grain boundary strengthening (k_y) in the AlCrFeNi lead to its higher YS than the CoCrFeMnNi and CoCrNi alloys. Nevertheless, more accurate comparison among these Hall-Petch parameters requires further efforts. Lastly, the minor Al element in AlCrFeNi alloy offers extra solid solution strengthening (due to Al's larger atomic size than others), which,

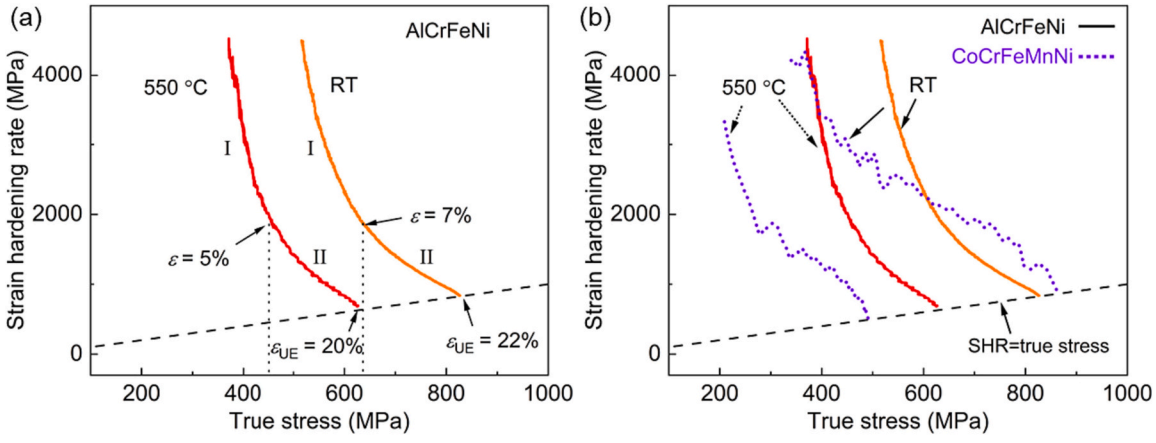

Fig. 3. (a) Representative strain hardening rate (SHR) *versus* true stress curves of the AlCrFeNi alloy tested at RT and 550 °C, and (b) corresponding comparison to CoCrFeMnNi alloy (in dotted lines). The dashed lines refer to the conditions for meeting Considere's criterion (*i.e.*, SHR true stress).

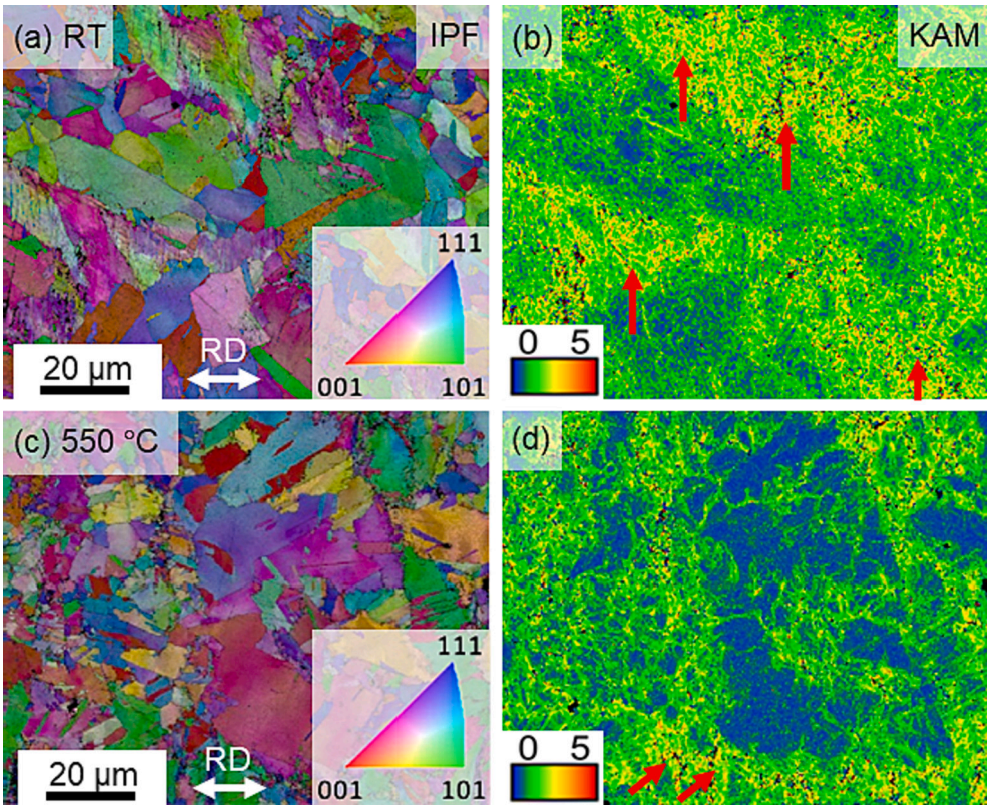

Fig. 4. EBSD results of the AlCrFeNi alloy tested at (a-b) RT, and (c-d) 550 °C. Figures in the left column are IPF (overlaying with IQ) maps along the rolling direction (RD), and the right ones are their corresponding KAM maps.

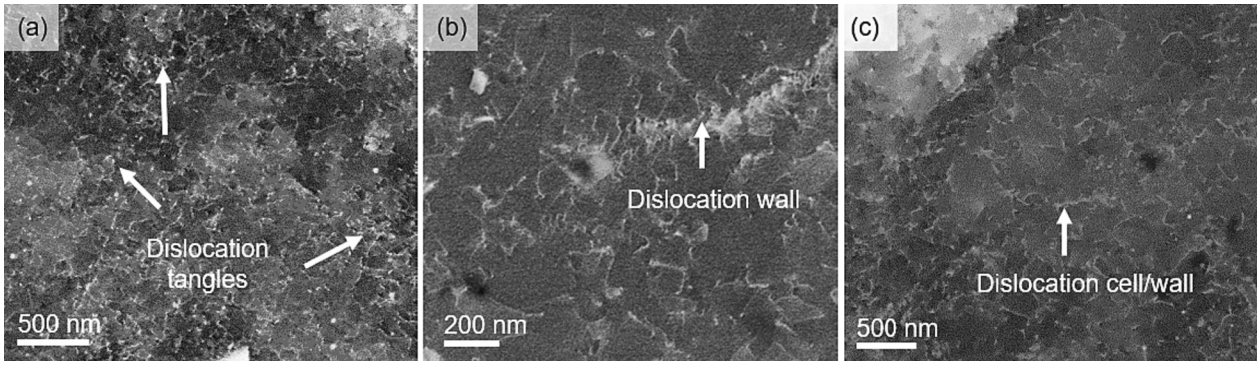

Fig. 5. Representative ECCI micrographs of the AlCrFeNi alloy tested at RT.

Table 2
Hall-Petch parameters σ_0 and k_y of the CrFeNi [11], CoCrNi [37] and CoCrFeMnNi [28] at RT.

Materials	Friction stress, σ_0 (MPa)	Hall-Petch constant, k_y (MPa μm$^{1/2}$)
CrFeNi	80	966
CoCrNi	150	815
CoCrFeMnNi	125	494

together with higher strain hardening, contributes to its higher YS than equiatomic CrFeNi.

4. Conclusions

In this study, mechanical deformation behaviors of a partially-recrystallized FCC $Al_6Cr_{25}Fe_{34}Ni_{35}$ (referred to as AlCrFeNi) MPEA were investigated at RT and 550 °C, and were further compared to those of other FCC MPEAs (including CoCrFeMnNi, CoCrNi and CrFeNi). The main conclusions are summarized as follows:

1) As compared to CoCrFeMnNi, the AlCrFeNi alloy shows higher strength-ductility combination at room temperature and 550 °C, *i.e.*, higher yield strength (by ~35%–47%), ultimate tensile strength and comparable ductility. The yield strength of AlCrFeNi is also increased (by ~27%) as compared to equiatomic CoCrNi and CrFeNi model MPEAs.
2) The deformed microstructures of the AlCrFeNi alloy exhibit high density of dislocation tangles and walls/cells, which are correlated with the observed stage I and II strain hardening, respectively (despite the fact that dislocation cells are often linked with stage I behavior). These dislocation substructures are believed to provide

high strain hardening capability, and ensure high tensile strength and excellent ductility of this alloy.

3) The AlCrFeNi's higher yield strength is mainly attributed to its higher strain hardening capability (stemming from its partially recrystallized microstructures) and higher grain boundary strengthening (*i.e.*, larger Hall-Petch slope) than CoCrNi and CoCrFeMnNi. In addition to the high strain hardening capability, extra solid solution strengthening (due to the presence of large atomic-sized Al) in AlCrFeNi alloy also contributes to its higher yield strength than CrFeNi alloy.

Therefore, this study not only offers mechanical properties and deformation mechanisms of a novel Co-free and low-cost AlCrFeNi alloy, but also provides methods to optimize FCC MPEAs (as well as austenitic stainless steels), such as by adding large sized atoms (*e.g.*, Al) and/or introducing partially-recrystallized microstructures.

CRediT authorship contribution statement

Kaiju Lu: Conceptualization, Data curation, Formal analysis, Investigation, Methodology, Writing – original draft. **Hao Shi:** Conceptualization, Formal analysis, Investigation, Methodology, Writing – review & editing. **Alfons Weisenburger:** Conceptualization, Methodology, Resources, Writing – review & editing. **Jarir Aktaa:** Conceptualization, Funding acquisition, Methodology, Resources, Supervision, Writing – review & editing.

Declaration of Competing Interest

The authors declare that they have no known competing financial interests or personal relationships that could have appeared to influence the work reported in this paper.

Data availability statement

The raw and processed data required to reproduce these findings are available upon request to kaiju.lu@kit.edu.

Acknowledgement

The authors would like to acknowledge Dr. Xukai Zhang from MPIE for his kind help in preparing TEM samples and TEM investigations.

References

[1] E.P. George, D. Raabe, R.O. Ritchie, High-entropy alloys, Nat. Rev. Mater. 4 (2019) 515–534.
[2] D.B. Miracle, O.N. Senkov, A critical review of high entropy alloys and related concepts, Acta Mater. 122 (2017) 448–511.
[3] B. Gludovatz, A. Hohenwarter, D. Catoor, E.H. Chang, E.P. George, R.O. Ritchie, A fracture-resistant high-entropy alloy for cryogenic applications, Science 345 (6201) (2014) 1153–1158.
[4] D.D. Zhang, H. Wang, J.Y. Zhang, H. Xue, G. Liu, J. Sun, Achieving excellent strength-ductility synergy in twinned NiCoCr medium-entropy alloy via Al/ta co-doping, Journal of Materials Science & Technology 87 (2021) 184–195.
[5] X. Liu, H. Feng, J. Wang, X. Chen, P. Jiang, F. Yuan, H. Li, E. Ma, X. Wu, Mechanical property comparisons between CrCoNi medium-entropy alloy and 316 stainless steels, Journal of Materials Science & Technology 108 (2021) 256–269.
[6] D.D. Zhang, J.Y. Zhang, J. Kuang, G. Liu, J. Sun, The B2 phase-driven microstructural heterogeneities and twinning enable ultrahigh cryogenic strength and large ductility in NiCoCr-based medium-entropy alloy, Acta Mater. 233 (2022).
[7] N. Yao, T. Lu, K. Feng, B. Sun, R.-Z. Wang, J. Wang, Y. Xie, P. Zhao, B. Han, X.-C. Zhang, S.-T. Tu, Ultrastrong and ductile additively manufactured precipitation-hardening medium-entropy alloy at ambient and cryogenic temperatures, Acta Mater. 236 (2022), 118142.
[8] G. Laplanche, A. Kostka, C. Reinhart, J. Hunfeld, G. Eggeler, E.P. George, Reasons for the superior mechanical properties of medium-entropy CrCoNi compared to high-entropy CrMnFeCoNi, Acta Mater. 128 (2017) 292–303.
[9] G. Laplanche, A. Kostka, O. Horst, G. Eggeler, E.P. George, Microstructure evolution and critical stress for twinning in the CrMnFeCoNi high-entropy alloy, Acta Mater. 118 (2016) 152–163.
[10] K. Lu, A. Chauhan, D. Litvinov, A.S. Tirunilai, J. Freudenberger, A. Kauffmann, M. Heilmaier, J. Aktaa, Micro-mechanical deformation behavior of CoCrFeMnNi high-entropy alloy, Journal of Materials Science & Technology 100 (2022) 237–245.
[11] M. Schneider, G. Laplanche, Effects of temperature on mechanical properties and deformation mechanisms of the equiatomic CrFeNi medium-entropy alloy, Acta Mater. 204 (2021).
[12] D. Hua, Q. Xia, W. Wang, Q. Zhou, S. Li, D. Qian, J. Shi, H. Wang, Atomistic insights into the deformation mechanism of a CoCrNi medium entropy alloy under nanoindentation, International Journal of Plasticity 142 (2021), 102997.
[13] J. Rackwitz, Q. Yu, Y. Yang, G. Laplanche, E.P. George, A.M. Minor, R.O. Ritchie, Effects of cryogenic temperature and grain size on fatigue-crack propagation in the medium-entropy CrCoNi alloy, Acta Mater. 200 (2020) 351–365.
[14] K. Lu, A. Chauhan, A.S. Tirunilai, J. Freudenberger, A. Kauffmann, M. Heilmaier, J. Aktaa, Deformation mechanisms of CoCrFeMnNi high-entropy alloy under low-cycle-fatigue loading, Acta Mater. 215 (2021), 117089.
[15] K. Lu, F. Knöpfle, A. Chauhan, D. Litvinov, M. Schneider, G. Laplanche, J. Aktaa, Elevated-temperature cyclic deformation mechanisms of CoCrNi in comparison to CoCrFeMnNi, Scr. Mater. 220 (2022), 114926.
[16] A.G. Wang, X.H. An, J. Gu, X.G. Wang, L.L. Li, W.L. Li, M. Song, Q.Q. Duan, Z. F. Zhang, X.Z. Liao, Effect of grain size on fatigue cracking at twin boundaries in a CoCrFeMnNi high-entropy alloy, Journal of Materials Science & Technology 39 (2019) 1–6.
[17] D. Liu, Q. Yu, S. Kabra, M. Jiang, P. Forna-Kreutzer, R. Zhang, M. Payne, F. Walsh, B. Gludovatz, M. Asta, A.M. Minor, E.P. George, R.O. Ritchie, Exceptional fracture toughness of CrCoNi-based medium- and high-entropy alloys at 20 kelvin, Science 378 (6623) (2022) 978–983.
[18] B. Gludovatz, A. Hohenwarter, K.V. Thurston, H. Bei, Z. Wu, E.P. George, R. O. Ritchie, Exceptional damage-tolerance of a medium-entropy alloy CrCoNi at cryogenic temperatures, Nat. Commun. 7 (2016) 10602.
[19] C.E. Slone, C.R. LaRosa, C.H. Zenk, E.P. George, M. Ghazisaeidi, M.J. Mills, Deactivating deformation twinning in medium-entropy CrCoNi with small additions of aluminum and titanium, Scr. Mater. 178 (2020) 295–300.
[20] D.D. Zhang, J.Y. Zhang, J. Kuang, G. Liu, J. Sun, Superior strength-ductility synergy and strain hardenability of Al/ta co-doped NiCoCr twinned medium entropy alloy for cryogenic applications, Acta Mater. 117288 (2021).
[21] K. Lu, F. Knöpfle, A. Chauhan, H.T. Jeong, D. Litvinov, M. Walter, W.J. Kim, J. Aktaa, Low-cycle fatigue behavior and deformation mechanisms of a dual-phase Al0.5CoCrFeMnNi high-entropy alloy, International Journal of Fatigue 163 (2022), 107075.
[22] C.E. Slone, J. Miao, E.P. George, M.J. Mills, Achieving ultra-high strength and ductility in equiatomic CrCoNi with partially recrystallized microstructures, Acta Mater. 165 (2019) 496–507.
[23] Z. An, S. Mao, Y. Liu, L. Yang, A. Vayyala, X. Wei, C. Liu, C. Shi, H. Jin, C. Liu, J. Zhang, Z. Zhang, X. Han, Inherent and multiple strain hardening imparting synergistic ultrahigh strength and ductility in a low stacking faulted heterogeneous high-entropy alloy, Acta Mater. 243 (2023).
[24] Q. Pan, L. Zhang, R. Feng, Q. Lu, K. An, A.C. Chuang, J.D. Poplawsky, P.K. Liaw, L. Lu, Gradient-cell-structured high-entropy alloy with exceptional strength and ductility, Science 0 (0) (2021) eabj8114.
[25] H. Shi, A. Jianu, R. Fetzer, D.V. Szabó, S. Schlabach, A. Weisenburger, C. Tang, A. Heinzel, F. Lang, G. Müller, Compatibility and microstructure evolution of Al-Cr-Fe-Ni high entropy model alloys exposed to oxygen-containing molten lead, Corros. Sci. 189 (2021).
[26] A.S. Tirunilai, J. Sas, K.-P. Weiss, H. Chen, D.V. Szabó, S. Schlabach, S. Haas, D. Geissler, J. Freudenberger, M. Heilmaier, A. Kauffmann, Peculiarities of deformation of CoCrFeMnNi at cryogenic temperatures, J. Mater. Res. 33 (19) (2018) 3287–3300.
[27] K. Lu, A. Chauhan, D. Litvinov, J. Aktaa, Temperature-dependent cyclic deformation behavior of CoCrFeMnNi high-entropy alloy, Int. J. Fatigue 160 (2022), 106863.
[28] F. Otto, A. Dlouhý, C. Somsen, H. Bei, G. Eggeler, E.P. George, The influences of temperature and microstructure on the tensile properties of a CoCrFeMnNi high-entropy alloy, Acta Mater. 61 (15) (2013) 5743–5755.
[29] M.A. Meyers, K.K. Chawla, Mechanical Behavior of Materials, Cambridge University Press, 2008.
[30] G. Saada, P. Veyssière, Chapter 61 Work hardening of face centred cubic crystals. Dislocations intersection and cross slip, in: F.R.N. Nabarro, M.S. Duesbery (Eds.), Dislocations in Solids, Elsevier, 2002, pp. 413–458.
[31] I. Gutierrez-Urrutia, D. Raabe, Multistage strain hardening through dislocation substructure and twinning in a high strength and ductile weight-reduced Fe–Mn–Al–C steel, Acta Mater. 60 (16) (2012) 5791–5802.
[32] H. Mughrabi, Dislocation wall and cell structures and long-range internal stresses in deformed metal crystals, Acta Metall. 31 (9) (1983) 1367–1379.
[33] T. Yang, Y.L. Zhao, Y. Tong, Z.B. Jiao, J. Wei, J.X. Cai, X.D. Han, D. Chen, A. Hu, J. J. Kai, K. Lu, Y. Liu, C.T. Liu, Multicomponent intermetallic nanoparticles and superb mechanical behaviors of complex alloys, Science 362 (6417) (2018) 933–937.
[34] K. Lu, A. Chauhan, F. Knöpfle, J. Aktaa, Effective and back stresses evolution upon cycling a high-entropy alloy, Materials Research Letters 10 (6) (2022) 369–376.

[35] Y.L. Zhao, T. Yang, J.H. Zhu, D. Chen, Y. Yang, A. Hu, C.T. Liu, J.J. Kai, Development of high-strength co-free high-entropy alloys hardened by nanosized precipitates, Scr. Mater. 148 (2018) 51–55.
[36] J. Gao, S. Jiang, H. Zhao, Y. Huang, H. Zhang, S. Wang, G. Wu, Y. Wu, H. Wu, A. Davydov, W.M. Rainforth, Z. Lu, X. Mao, Enhancing strength and ductility in a near medium Mn austenitic steel via multiple deformation mechanisms through nanoprecipitation, Acta Mater. 243 (2023).
[37] M. Schneider, E.P. George, T.J. Manescau, T. Záležák, J. Hunfeld, A. Dlouhý, G. Eggeler, G. Laplanche, Analysis of strengthening due to grain boundaries and annealing twin boundaries in the CrCoNi medium-entropy alloy, Int. J. Plast. 124 (2020) 155–169.